Materials for Renewable and Sustainable Energy
https://doi.org/10.1007/s40243-023-00237-4

ORIGINAL PAPER

Low-temperature synthesis of doped MnO_2–carbon dots nanocomposite: an analysis of nanostructure and electrical properties

E. Hastuti[2] · F. Fitriana[3] · M. Zainuri[1] · S. Suasmoro[1]

Received: 23 March 2023 / Accepted: 22 June 2023

Abstract
The synthesis of δ-MnO_2, δ-MnO_2 carbon dots nanocomposite, and Fe/Cu-doped δ-MnO_2 carbon dots nanocomposite has been successfully carried out through a stirring process at room temperature and 80 °C. The synthesized powder shows a low crystallization determined through XRD and TEM analysis. Furthermore, the carbon dots are well attached to MnO_2 performing a core–shell composite material, while the doping ions Fe and Cu were incorporated into the matrix substitute Mn in the MnO_6 octahedron, although potassium ions were also detected. The manganese possess an oxidation state of + 3 and + 4, which promotes the oxygen vacancy creation $V_O^{\cdot\cdot}$ denoting the conductivity decrease.

Keywords Manganese oxide · Low temperatures · Synthesis · Nanocomposite · Oxidation state

Introduction

The use of fossil energy nowadays is being worked on to minimize its utilization due to causing a problem, i.e., is a limited source and the root of an environmental issue. The use of alternate energy becomes intriguing. Correspondingly, the need for adequate energy storage in the sense of highly possessing power and energy density becomes imperative, such as batteries and supercapacitors. In supercapacitors, the charge–discharge cycle mechanism and charge stored are reversible. Metallic oxide is an alternative for an electrode material that holds high specific capacitance and low resistivity. Typical metal oxide materials were reported, RuO_2, MnO_2, NiO, Co_3O_4, and $NiCo_2O_4$ [1]. Manganese oxide is among the most interesting due to its high theoretical specific capacitance (1370 F gr^{-1}), low cost, and environmentally friendly [2].

Given the structure, manganese oxide behaves in polymorph structures α, β, γ, δ, and λ-type MnO_2. The polymorphism can be described by the number of octahedral sub-units ($n \times m$), where n and m stand for the dimensions of the tunnels in the two directions perpendicular to the chains of the edge-sharing octahedral MnO_6. The α-type structure is characteristic of (2 × 2) and (1 × 1) of MnO_6 octahedra units aligned along the c-axis. The β-MnO_2 is characterized by one-dimensional chains of MnO_6 octahedra aligned along the c-axis to form (1 × 1) size vacant tunnels. γ-MnO_2 type structure is an intergrowth structure consisting of (2 × 1) and (1 × 1) tunnels. The δ-type MnO_2 has a layered structure; each layer is composed of edge-sharing MnO_6 octahedra. Finally, the λ-type MnO_2 has a defective spinel structure [3]. It was reported that these structures possess thermal stability order β > α > γ > δ ≈ λ [4].

The use of MnO_2 as charge storage was involved in the capability of the manganese oxidation state alteration Mn^{3+} and Mn^{4+} inside the octahedron MnO_6 presenting defect [5], and hence, the storage capacity can be improved through doping creating defects. Metallic ions, such as V, Ru, Ag, Co, Ni, Sn, Cu, and Fe, were reported as successful dopants for Mn [16, 17, 22, 23]. Previous studies revealed that Fe- and Cu-doped α-MnO_2 [6, 7], both Fe and Cu present a mixed oxidation state Fe^{+3}, Fe^{4+}, and Cu^{2+}, Cu^{3+}, while Mn^{3+}, Mn^{4+}. This creates defects Fe'_{Mn}, Cu'_{Mn}, Mn'_{Mn}, and $V_O^{\cdot\cdot}$. The Cu^{2+} has large size, may filled tunnel (2 × 2) otherwise substitute Mn creating Cu''_{Mn}. Given the dopant percentage, 5% of dopant Cu and Fe is the plausible characteristics in view of conductivity and permittivity.

✉ S. Suasmoro
S.Suasmoro.suasm@its.ac.id

[1] Institute of Technology 'Sepuluh Nopember' Surabaya, Kampus ITS Sukolilo, Surabaya 60111, Indonesia

[2] Universitas Islam Negeri 'Maulana Malik Ibrahim' Malang, Malang, Indonesia

[3] Universitas Negeri Surabaya, Surabaya, Indonesia

Published online: 04 August 2023

Moreover, decreases in the average crystallite size have two effects, reduce the appearance of lattice strain, increase the effective surface area, and finally facilitate the charge transfer during the charging and discharging processes. In parallel, to increase the conductivity, carbon-based material was usually used as an improver [8]. Several types of supercapacitors were reported, among them was a carbon base supercapacitor developed through an electric double-layer capacitor (EDLC) to include carbon nanotubes (CNTs), activated carbon, carbon black, and carbon fiber [9–11]. On the other hand, carbon dots (CDs) have a small dimension (≈ 10 nm) which is considerable attribute including enhanced electron transferability, long-term chemical stability, negligible toxicity, and acquaintance of large effective surface area-to-volume ratio [12]. Nanostructures and composite material engineering are effective methods for improving electrode capacitive performance. The core–shell structure has been shown to be an effective technique for improving the electrochemical performances of nanocomposites, resulting in improved electrical conductivity, shorter ionic transport, and stronger bonds [13]. Given the good sense above, the material composed of MnO_2-doped containing carbon should be expected to give an exceptional characteristic.

Various synthesis methods have been reported, i.e., sol–gel [14], coprecipitation [15], electrodeposition [16], hydrothermal reaction [17], and oxidation–reduction (Redox) method [18]. The redox reaction is a simple method for producing selective MnO_2 with high specific capacitance. The production of MnO_2 by such a process has the benefit of being a very rapid, one-pot reaction that is performed at a low temperature and takes shorter, and the technique is fulfilled by basic laboratory equipment [19]. Given the previous synthesis methods, it is intriguing to pursue the synthesis of doped MnO_2/CDs nanocomposites at low temperatures to simplify synthesis suitable to electrochemical storage such as supercapacitors. To discover the description of the synthesized powder, MnO_2/CDs' nanocomposite that will be synthesized based on a redox reaction between Mn^{2+} and Mn^{4+}, mixed with CDs and further 5% of the metal transition Fe^{3+} and Cu^{2+} as dopants.

Materials and methods

Materials' preparation

Synthesis of carbon dots (CDs)

The CDs were completed using a one-step hydrothermal process with glucose, and 6 g of glucose were dissolved in 60 ml of deionized water by stirring for 30 min. The solution was then transferred to a 100-ml stainless-steel autoclave with a Teflon lining, which was subsequently put in a 180 °C oven for 2 h. The autoclave was naturally cooled to room temperature, and the CD solvent was acquired. After the hydrothermal treatment, the translucent suspension turns brown. The produced brown suspension was centrifuged at 4500 rpm for 15 min and filtered through a 0.22-µm filter.

Synthesis of δ-MnO_2

In this study, we applied a mixed oxidation–reduction process using $MnCl_2$ and $KMnO_4$ to synthesize δ-MnO_2, following the redox reaction:

$$\mathbf{3}MnCl_2 + \mathbf{2}KMnO_4 + \mathbf{6}H_2O \rightarrow \mathbf{5}MnO_2 + \mathbf{2}KCl + \mathbf{4}HCl + \mathbf{4}H_2O. \quad (1)$$

In a typical MnO_2 synthesis, 0.712 g of $MnCl_2.4H_2O$ was ultrasonically dissolved in 60 ml of distilled water for 1 h. Following that, 0.948 g of $KMnO_4$ was added to this solution, which was then stirred for about 10 min at room temperature and continued for 1 h at 80 °C, and the pink color of permanganate changed to brownish-black. The product was washed several times with deionized water and ethanol until the filtrate became neutral, then dried at 80 °C for 2 h. The sample δ-MnO_2 was referred to as M-0 and MS for stirring at room temperature and 80 °C, respectively.

Synthesis of δ-MnO_2/CDs nanocomposites and doped samples

Because of the thin-layered structure of graphene [20], almost all of the carbon atoms are reactive; thus, it can be oxidized by MnO_4^- ions in an acid solution via the following chemical reaction:

$$MnCl_2 + 2KMnO_4 + (1+x)C + 2H_2O \rightarrow 3MnO_2 + xC + HCl + H_2O + KHCO_3. \quad (2)$$

Given the thin carbon dot (CDs) size, it is expected that the above reaction will occur in the case of MnO_2/CDs ($MnO_2 + xC$). In this procedure, 7.12 ml CDs solution was added to a solution of $MnCl_2.4H_2O$, followed by a similar preparation as above. MnO_2/CDs nanocomposites were made using the stirring method at low temperatures (room temperature and 80 °C). The products are abbreviated as MC-0 and MCS. The schematic of this process is shown in Fig. 1. To synthesize Fe- and Cu-doped nanocomposite samples, $FeCl_3 \cdot 6H_2O$ and $CuCl_2 \cdot 2H_2O$ (5 mol%) were used as dopant reagents and added to the above solution and proceeded similarly.

Characterization

The phase and crystal structure of MnO_2 were investigated using X-ray diffraction (XRD Philips X'Pert) with Cu–K

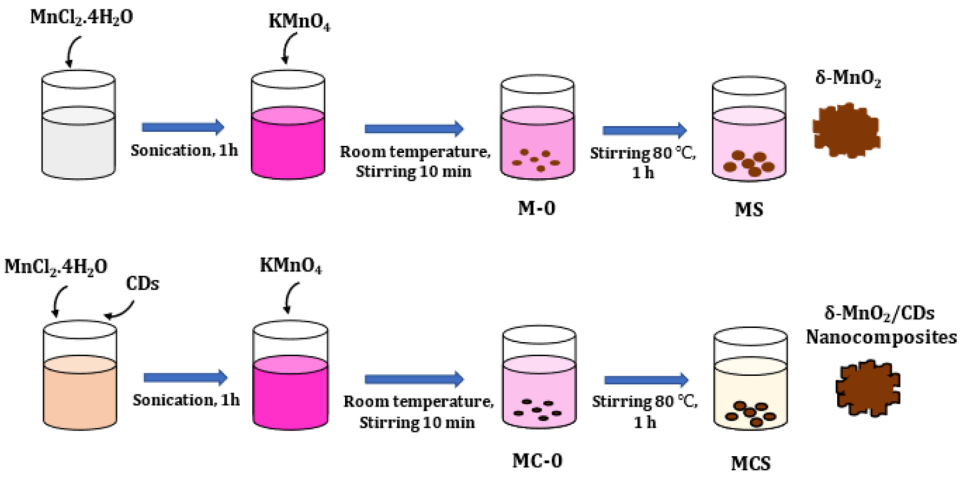

Fig. 1 The schematic of the synthesis procedure for MnO_2 and MnO_2/CDs' nanocomposites

radiation at 30 mA and 40 kV, step scan 0.02°, and Bragg angle range of 5°–60°. Through the match, phase identification was accomplished! Software. Fast Fourier transform infrared (FTIR) measurements were used to determine the chemical structure of MnO_2 and nanocomposites.

Field emission scanning electron microscope (FESEM) images and other element maps involving energy-dispersive X-ray (EDX) analysis were used to determine the morphology. Using ImageJ software, the numerical dimension of each sample was obtained by averaging the diameters of nanorods from different samples.

X-ray photoelectron spectroscopy (XPS) analysis data were obtained with an Axis Ultra DLD system equipped with an Al monochromatic was carried out to analyze the oxidation state of Mn and other elements in the sample.

Electrical measurements were taken on powder that was inserted between two copper electrodes and then uniaxially pressed with a 13 mm diameter. The data were collected using a Solartron Impedance Analyzer SI 1260 at room temperature with a frequency range of 0.1 Hz to 32 MHz and an applied voltage of 1 V.

Results and discussion

Powder assessment using X-ray diffraction and FTIR

X-ray diffraction (XRD) studies have been used to identify the presence of the different phases/purity of synthesized MnO_2 and MnO_2/CD nanocomposites. The X-ray diffraction spectra of the MnO_2 and MnO_2/CDs composite mixed at room temperature are presented in Fig. 2a. It is noted that diffraction peaks show broad peaks at 2θ around 37°, which can be indexed to δ-type MnO_2 (JCPDS 42-1317). Further analysis, the γ-type MnO_2 (JCPDS 14-0644) [21] seems to be matched with the spectra MC0. It was reported that in processing at low temperatures [3], either γ-phase or δ-phase was formed. Therefore, it can be considered as a mixed phase of δ and γ-MnO_2. Broad peaks are related to a coincidence of diffraction peaks of (110) of the δ phase and (131) of the γ phase, besides, a poorly crystallized compound originating from the small grain size and approximately amorphous state of the powder. The δ-phased MnO_2 is a 2D layered structure with an interlayer separation of ~ 7 Å between the MnO_6 octahedra, in which a large number of stabilizing cations, such as K^+ and H^+, were considered to fill those spaces. While the γ-MnO_2 contains octahedrons chain corner and edge-sharing producing (2×1) and (1×1) tunnel. In another disparity treatment, the sample was then stirred at a temperature of 80 °C for an hour. The spectra of X-ray diffraction on MnO_2 samples, MnO_2/CDs' nanocomposites, and Cu- and Fe-doped samples are shown.

XRD patterns confirm MnO_2/CDs with mixed crystalline and amorphous parts, δ-MnO_2 and γ-MnO_2 exhibited low intensity and broad diffraction peaks at 37°, which is typical of hexagonal randomly stacked and single-phased Birnessite-type MnO_2 [23]. The diffraction peaks of MCS had not changed when compared to MnO_2. The MnO_2/CDs were no longer pure MnO_2 phases, but the contours of the peaks were nearly identical. Therefore, it can be concluded that the presence of CDs does not change the crystal structure of MnO_2.

Further investigation was conducted by FTIR measurements to characterize the chemical structure of MnO_2 and nanocomposites. Figure 2b shows the FTIR spectra of MnO_2 and MnO_2/CDs with different methods of preparation, i.e., stirred at room temperature and 80 °C. The peaks presented at 518 cm^{-1} and 524 cm^{-1} are attributed to the stretching vibrations of Mn–O–Mn. A broad peak centered at 3444 cm^{-1} and a shoulder peak at 1645 cm^{-1} reveal the existence of hydroxyl groups on the surfaces of materials. The existence of CDs was demonstrated by the characteristic absorption at 1200 cm^{-1} in which the former was signed to the C=C vibrational stretch. The undetected signal of Cu and

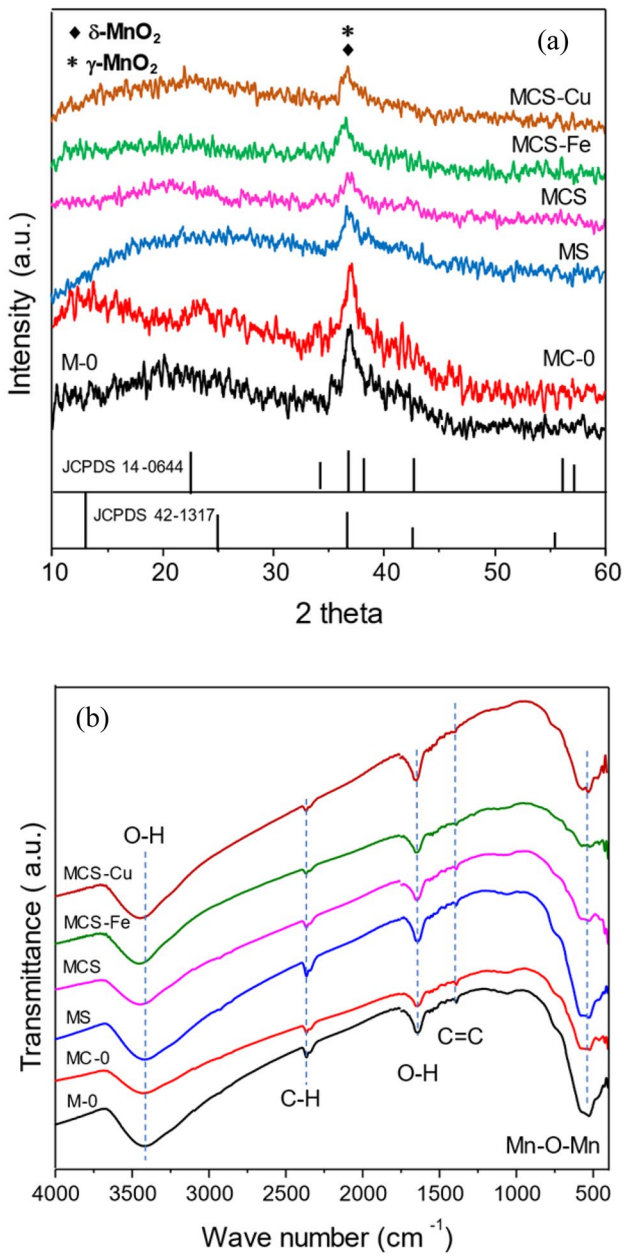

Fig. 2 **a** XRD pattern of MnO_2 and MnO_2/CDs prepared at room temperature (M-0, MC-0); prepared by stirring at 80 °C for 1 h MnO_2 (MS), MnO_2/CDs (MCS), Fe-doped MnO_2/CDs (MCS-Fe), and Cu-doped MnO_2/CDs (MCS-Cu); **b** FTIR pattern of similar samples in **a**

Fe dopants should be considered that its low concentration and substitute Mn in BO_6 octahedron makes it signal covered by Mn–O–Mn-stretching vibration.

Microstructure and structure analysis through FESEM/TEM

Field emission scanning electron microscope (FESEM) analysis is used to decipher the surface morphology of the as-obtained δ-MnO_2 and composites material (Fig. 3a). All sample shows spherical morphology with a flower-like type of nanostructures, with a diameter of about 300 nm. The addition of CDs to MnO_2 causes the surface of the nanocomposite's appearance to be smoother, which indicates the presence of CDs attached to the surface of MnO_2.

Further analysis using EDX, Fig. 3b shows the MCS-Fe sample for representatives, and the similar fashion for other samples should be referred to supplement Fig. 1S. It was observed the K^+ ion residue on all synthesized materials, which may fill in between layers due to its ionic size makes K^+ not substitute Mn^{4+} in MnO_6 octahedron. Dopants Fe and Cu were detected which indicates that dopants were incorporated in the MnO_2 matrix a priori substitute Mn in MO_6 octahedron. Furthermore, carbon was also detected, which confirmed the FTIR and FESEM analysis given previously.

Further detailed analysis insight into the morphology, TEM analysis, and SAED were used in MC's samples. Figure 4 shows the shape of the morphology of MCs that flower type which is similar to that of FESEM. Furthermore, at higher magnifications up to 300.000 × (Fig. 4b), the grains are observed as typically elongated nanorods of the dimension ≈ 2 nm (width) and ≈100 nm (length) and shortened in Fe/Cu-doped sample. It is also the core cell type grains shown by the MCS sample (Fig. 4b inset) that signifies MnO_2 grains are covered by CDs, while non-carbonated sample MS are absent from carbon cells. This occurrence reinforces the analysis given by FESEM and EDX previously.

The SAED pictures show a circles fringe indicating polycrystal diffraction and are indexed as (110) and (020) reflection planes of δ-MnO_2 (Table 1); however, a wide fringe is presented which is an indication of low crystalline arrangement; otherwise, the coincidence of the reflection plane owing to γ-MnO_2 as described in XRD analysis previously and CDs coated grains.

XPS analysis

The elemental composition and surface functional group types of δ-MnO_2 (MS), δ-MnO_2/CDs composite (MCS), and Fe/Cu-doped MnO_2/CDs (MCS-Fe, MCS-Cu), as well as the state of Mn and O in the materials were studied using XPS. Figure 5 shows the MCS-Fe sample of the XPS survey spectrum and the deconvolution of selected peaks high-resolution spectrum of Mn3s, C1s, O1s, Mn2p, and Fe2p. Further data should be referred to in Fig. 2S. It demonstrates that the composite is primarily made up of the elements Mn, C, and O. The high-resolution XPS of Mn2p is shown in Fig. 5e (so did for other samples depicted in Fig. 2S); there are three distinct characteristic peaks at 641.92 eV, 643.75 eV, 653.52 eV, and 654.35 eV which are indexed to $Mn2p_{3/2}$ and $Mn2p_{1/2}$, respectively (Table 2). While the

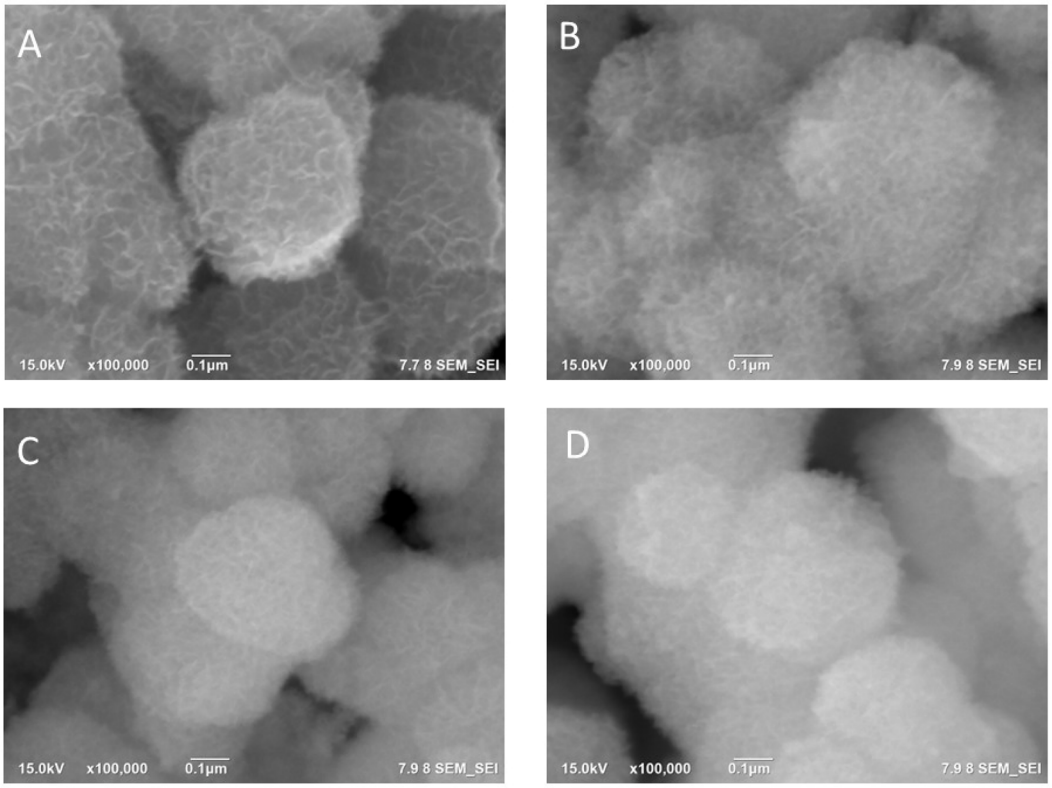

(a)

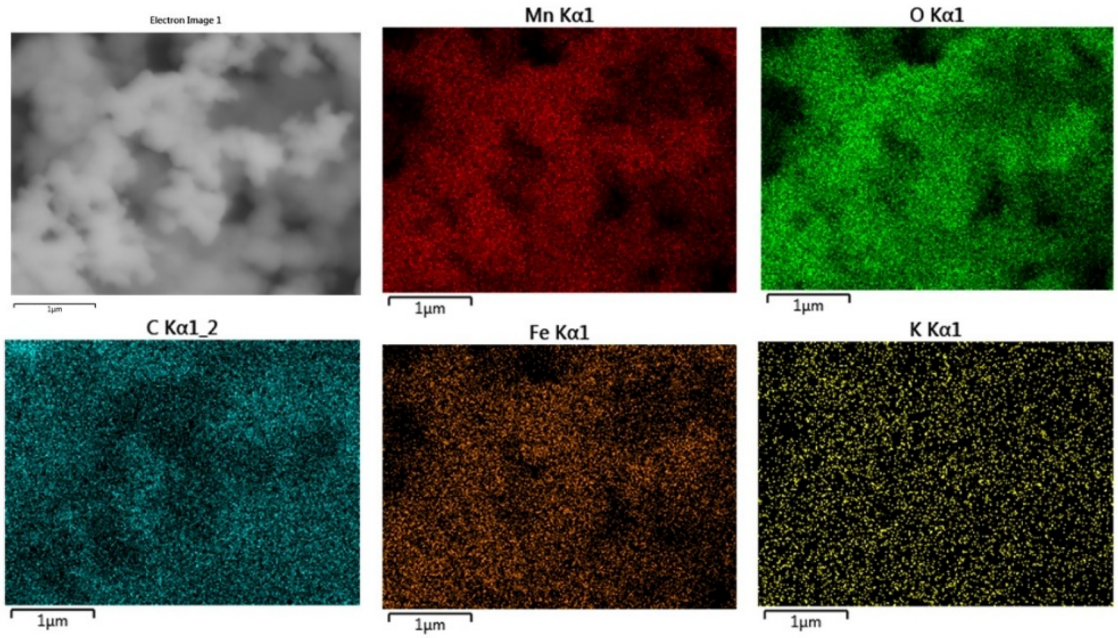

(b)

Fig. 3 **a** FESEM of synthesized samples: (A) MS, (B) MCS, (C) MCS-Fe, and (D) MCS-Cu; **b** the EDX maps of the MCF/CDs sample

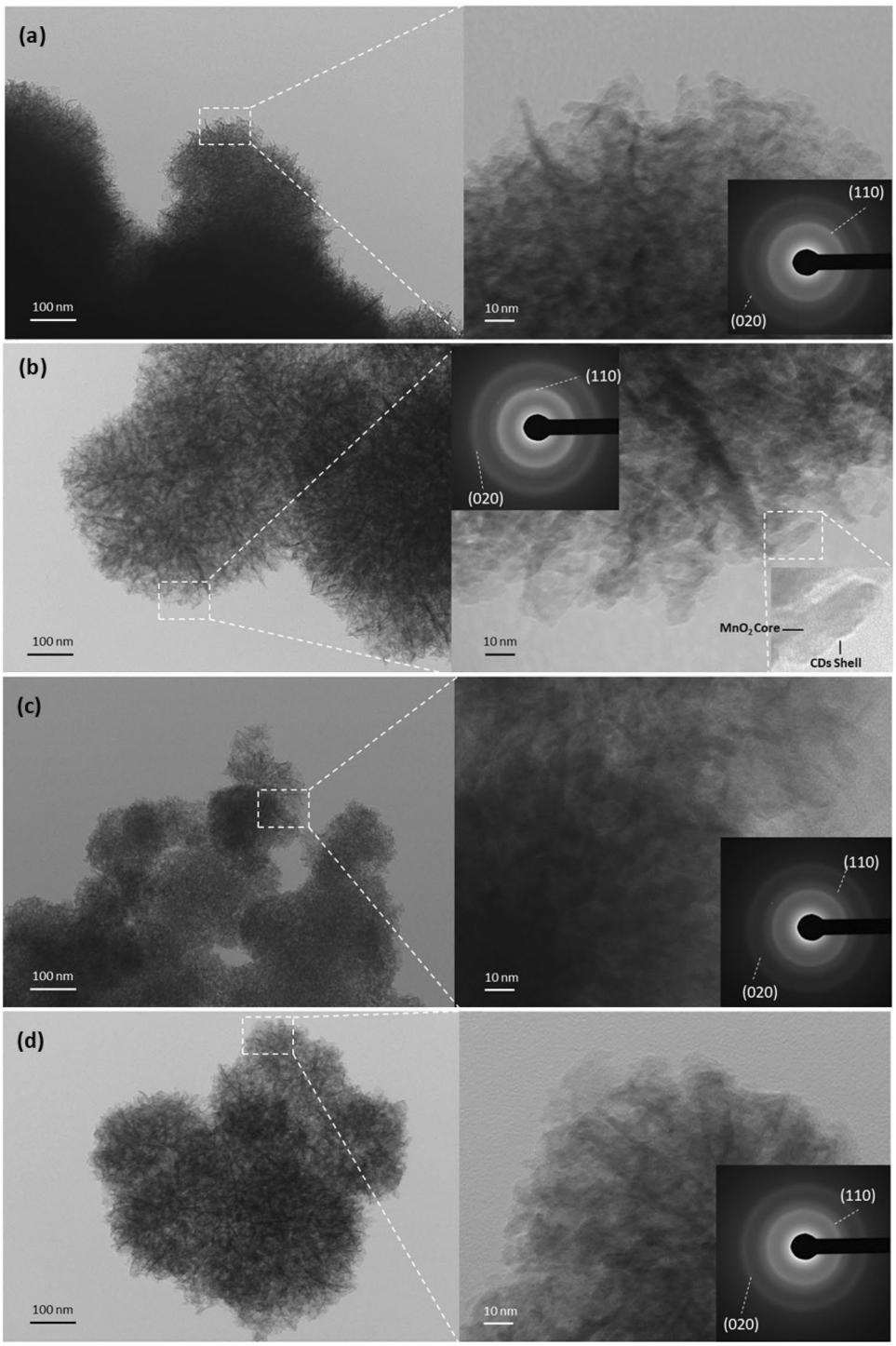

Fig. 4 TEM image of low magnification (left) and SAED of samples: **a** MS, **b** MCS, **c** MCS-Fe, and **d** MCS-Cu

Table 1 SAED data of MS, MCS, MCS-Fe, and MCS-Cu

Sample	MS		MCS		MCS-Fe		MCS-Cu	
d_{hkl} (Å)	2.508	1.524	2.564	1.535	2.671	1.553	2.631	1.583
(*hkl*)	(110)	(020)	(110)	(020)	(110)	(020)	(110)	(020)

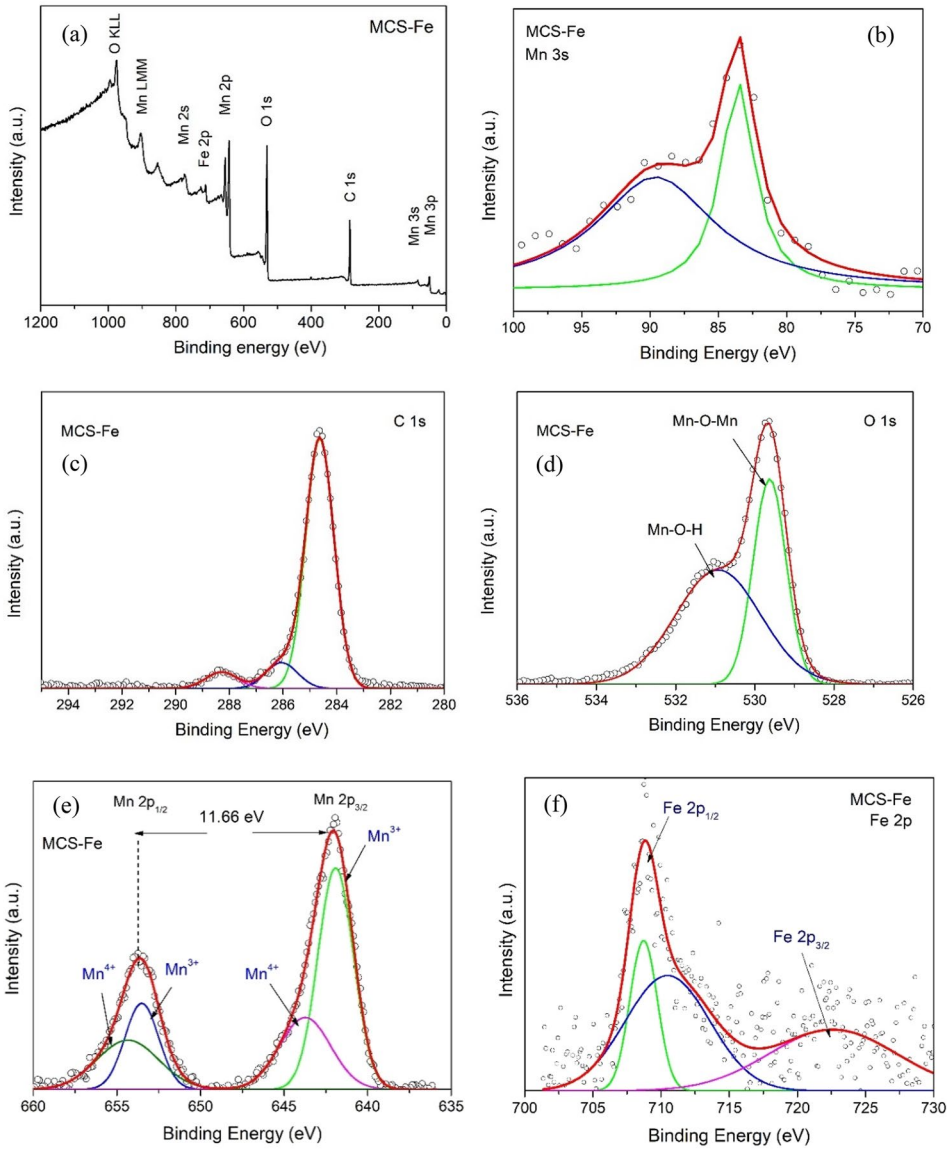

Fig. 5 XPS survey spectra of MSC-Fe sample and deconvolution of selected peaks C 1 s, O 1 s, Mn 2p, and Fe 2p

energy difference between $Mn2p_{3/2}$ and $Mn2p_{1/2}$ characteristic peaks is 11.80 eV, it proves the presence of Mn in the form of + 3 and + 4 valence in the composite material. Based on high-resolution XPS spectra of Mn2p and O1s, it can be decided that the Mn element in the composite is in the form of MnO_2.

The Mn 3 s is used to calculate the average oxidation state of Mn, with reducing energy separation among the 7 S and 5 S multiplet associated with an increasing oxidation state [24]. From the deconvolution process using Gaussian function, Mn3s spectrum analysis (Fig. 5b), possessing a spin-energy splitting of 4.77, 4.57, and 5.03 eV and using Beyreuther equation [25], revealed the average oxidation state of Mn are 2.832, 3.594, 2.009, and 2.648 5.384, 4.784, 6,032 and 5.529 for MS, MCS, MCS-Fe, and MCS-Cu, respectively. This demonstrates that the average oxidation states (AOS) of Mn are Mn^{3+} and Mn^{4+}. All deconvolution of Mn 2p peaks as well as the AOS are presented in Table 2.

The deconvoluted O1s spectrum (Fig. 5d) can be fitted with the presence of an Mn–O–Mn bond (cantered at 529.49 eV), and an Mn–O-H bond (531.1 eV) belonging to defect oxide or hydroxyl-like groups [26]. The lattice oxygen Mn–O–Mn content was gradually decreased with the carbon and dopant (Fe, Cu), with the areal of Mn–O-Mn over MS, MCS, MCS-Fe, and MCS-Cu summarized in Table 2. Another important difference in the O 1 s spectra of MCS nanocomposites compared to that of doping samples is the decrease in the relative intensity of peak, which can suggest a decrease in the number of Mn–O bonds. This may be due to the existence of Mn^{3+}, Fe^{2+}, Fe^{3+}, or Cu^{2+} species on the surface, indicating the possibility of oxygen vacancies in the sample.

Table 2 The XPS dates of Mn 2p and Mn 3 s values of MS, MCS, MCS-Fe, and MCS-Cu

Samples	Mn 2p			Mn 3 s		O 1 s
	Species	Peak (eV)	Energy gap (eV)	ΔE_{3s}	AOS	Area
MS	$2p_{3/2}$ (Mn^{3+})	642.13	11.74	5.384	2.832	3579.85
	$2p_{3/2}$ (Mn^{3+})	642.36				
	$2p_{3/2}$ (Mn^{4+})	644.52				
	$2p_{1/2}$ (Mn^{3+})	653.92				
	$2p_{1/2}$ (Mn^{4+})	655.14				
MCS	$2p_{3/2}$ (Mn^{3+})	642.22	11.64	4.784	3.594	8425.81
	$2p_{3/2}$ (Mn^{4+})	643.86				
	$2p_{1/2}$ (Mn^{3+})	653.94				
	$2p_{1/2}$ (Mn^{4+})	656.80				
MCS-Fe	$2p_{3/2}$ (Mn^{3+})	641.92	11.80	6,032	2.009	4375.51
	$2p_{3/2}$ (Mn^{4+})	643.75				
	$2p_{1/2}$ (Mn^{3+})	653.52				
	$2p_{1/2}$ (Mn^{4+})	654.35				
MCS-Cu	$2p_{3/2}$ (Mn^{3+})	643.77	11.66	5.529	2.648	1241.82
	$2p_{3/2}$ (Mn^{4+})	645.06				
	$2p_{1/2}$ (Mn^{3+})	653.44				
	$2p_{1/2}$ (Mn^{4+})	655.45				

Additionally, to study the structural configuration of carbon dots and their defects (such as vacancies and disorder) in MnO_2/CDs' nanocomposites, the C1s peak of MCS-Fe was deconvoluted into three peaks with binding energies of 284.73 eV is related to C = C/C–C graphitic structure (sp^2), 286.26 eV attributed to C–O in hydroxyls, epoxy groups, and phenols, and 288.09 eV associated with C=O/C–OOH in ketones, aldehydes, and quinones [27]. An addition of CDs has a significant effect on the composition of the C–C/C=C functional group. Meanwhile, Fe and Cu doping caused a level shift of binding energy that tend to interact between dopant and carbon and confirms the presence of defects and vacancies in this sample. The FWHM of nanocomposites varies in the range of 1–2.5 eV.

Deconvolution of Fe2p revealed the energy characteristic Fe^{3+} at 710.82 eV and 712.58 eV $2p_{3/2}$, while the $2p_{1/2}$ indicated Fe^{3+} at 724.71 eV. Furthermore, Cu 2p peaks, which include Cu $2p_{3/2}$ peak at 935.34 eV to satellite peaks at 947 eV, and the Cu $2p_{1/2}$ peak at 956.81 eV. In general, the presence of the Cu_2O phase is confirmed. The lack of this phase in the XRD pattern, on the other hand, suggests that its presence is limited to the surface layer and the creation of exposure to air and oxygen. Regardless, the most common oxidation state in this material is Cu^{2+}. Presumably, Fe^{2+}, Fe^{3+} and Cu^{2+} substitute Mn^{4+} in MO_6 octahedron creating defect Fe''_{Mn} Fe'_{Mn}, Cu''_{Mn}, and $V_O^{\cdot\cdot}$.

Electrical properties

The electrical circuit model of the arrangement described in paragraph 2.2. includes a wiring circuit, material response, and electrodes. However, given the attained data, the wiring and electrode response should be insignificant comparing the material response, and hence, the circuit model approach should become the serial of a parallel circuit of resistance and capacitance of grain and grain boundary. The electrical analysis therefore should be conducted using two methods: the Nyquist plot and the Debye plot based on the circuit model given in Fig. 6 (inset) of the material then deduced to the equation as depicted in Eqs. (3–5) [28]. The resistance R_1, R_2, and capacitance C_1, C_2 should be deduced through either impedance Z'–Z'' plot or Debye relaxation where ωRC's = 1 at the maximum of Z''(ω)

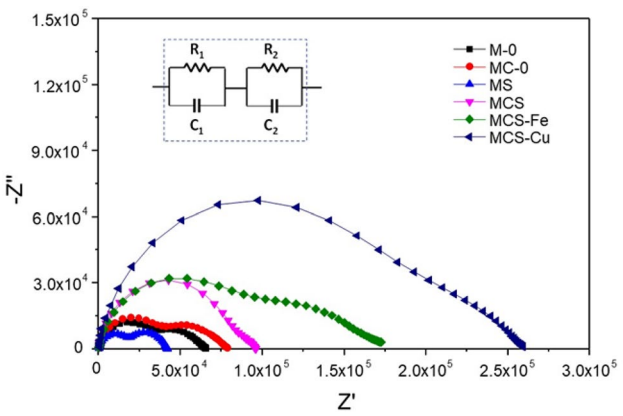

Fig. 6 Nyquist plot of real impedance Z' versus imaginary impedance Z'' of samples

$$Z^* = Z' + Z'', \tag{3}$$

$$Z' = \frac{R_1}{1 + \left(\omega R_1 C_1\right)^2} + \frac{R_2}{1 + \left(\omega R_2 C_2\right)^2}, \tag{4}$$

$$-Z'' = \frac{\omega {R_1}^2 C_1}{1 + \left(\omega R_1 \omega_1\right)^2} + \frac{\omega {R_2}^2 C_2}{1 + \left(\omega R_2 C_2\right)^2}. \tag{5}$$

Figure 6 depicts a Nyquist plot of real impedance Z' versus imaginary impedance Z'' for all samples, demonstrating the formation of negative Z' which signifies a capacitive response. Focusing on the material aspect, two semicircles are composed of grain resistance and capacitance, and grain boundary resistance and capacitance responses. The addition of CDs in the sample results in larger radius semicircles. The small semicircle observed in MS suggests that the electrical processes in the material arise because of grain material contribution. The semicircle radius increased dramatically in MCS-Fe and MCS-Cu samples, indicating that doping Fe and Cu results in the formation of defects that inhibit electron mobility, increasing resistance.

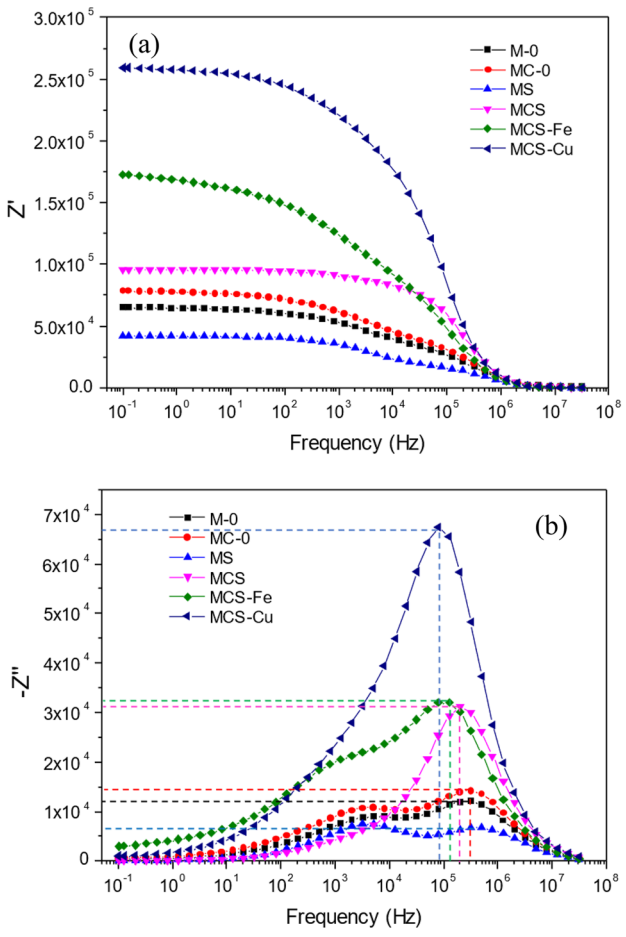

Fig. 7 Frequency dependence of **a** real impedance Z' and **b** imaginary impedance Z''

Figure 7a depicts the real impedance Z' component versus frequency. The amplitude of Z' is greater in the low-frequency region, decreases monotonically with increasing frequency, and then drops significantly above $f \approx 10^4$ Hz. Furthermore, the magnitude of Z' increases with the addition of CD and dopant, and its value for all samples combine in the higher frequency region. This could be due to the release of space charge polarization caused by the material's decreased barrier properties at high frequencies. Cu and Fe doping increases oxygen vacancies caused by the possibility of substitution of Fe^{3+}, Fe^{2+}, Cu^{2+}, and Cu^{+} on Mn^{4+}.

Figure 7b shows the frequency dependence of imaginary impedance Z'' at different composite, with a typical Debye relaxation curve at $f \approx 10^3$ Hz and $f \approx 10^5$ Hz, as well as the detailed numerical values of R_1 and R_2 determined by relaxation frequency. As shown in the graph, the Z'' value rises initially, reaches a peak Z'' max, and then falls with frequency. With the addition of CDs and dopants, the position of the Z'' peak increases and regularly shifts to a lower frequency, indicating a gathering of relaxation times in the system. Table 3 summarizes the numerical values of material resistance (R_1 and R_2) concluded by the Nyquist plot and Debye relaxation frequency, with a focus on the grain response of the Z' and Z''.

The permittivity of the material is related to the capacitance. The relative permittivity and phase as a function of frequency are depicted in Fig. 8 for various samples. All samples showed that dielectric constants reduced with increasing frequency before achieving constant values in the high-frequency region.

At low frequencies, space charge determines relative permittivity, whereas dipole polarization determines it at high frequencies. The unbounded electrons produced during defect reactions caused by unusually high relative permittivity are referred to as space charges. The presence of multiple defects in the material causes the formation of defect

Table 3 Grains resistance R_1 and R_2 of samples derived from Nyquist and Debye plots

Sample	R_1 (ohm)		R_2 (ohm)	
	'Nyquist'	'Debye'	'Nyquist'	'Debye'
M-0	23,400	24,000	18,900	18,000
MC-0	24,300	29,000	27,900	22,000
MS	17,100	11,600	11,700	10,800
MCS	47,700	62,000	10,800	12,000
MCS-Fe	64,700	64,000	41,400	42,000
MCS-Cu	120,000	134,000	52,000	40,000

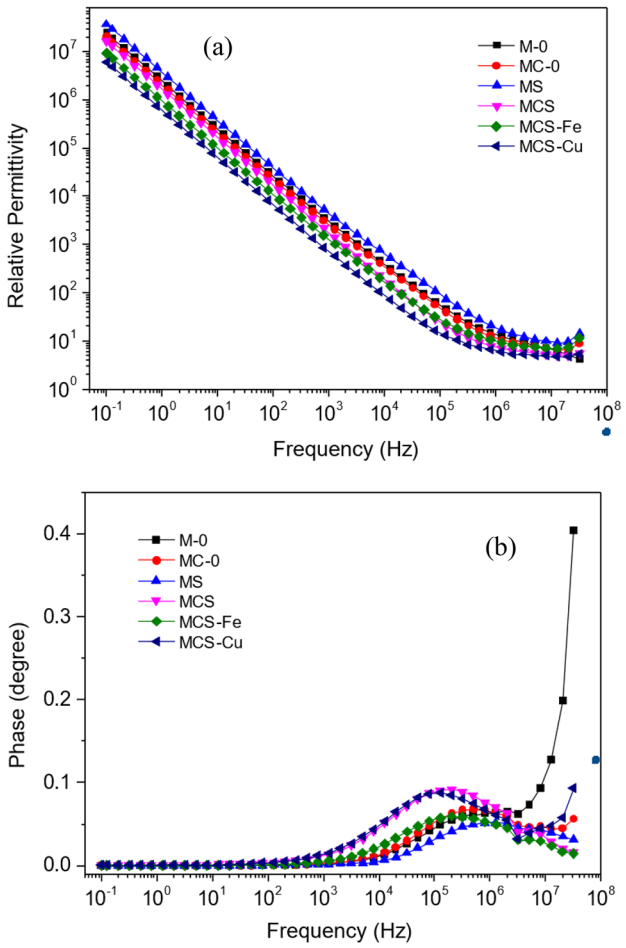

Fig. 8 Frequency dependence of **a** relative real permittivity ε' and **b** relative imaginary permittivity ε''

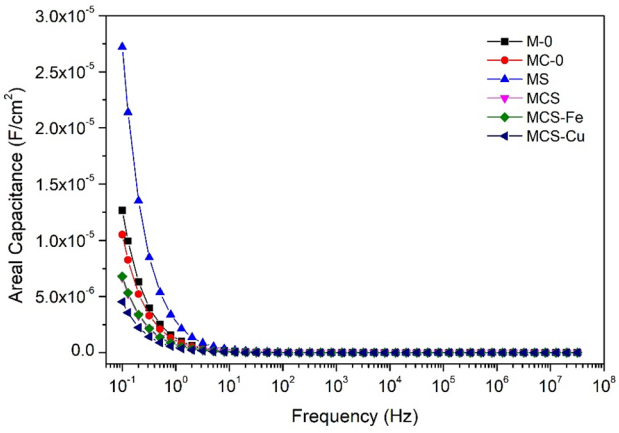

Fig. 9 The dependency frequency on the areal capacitance of samples

dipoles, which leap to face the high frequency of the external electric field, resulting in low permittivity.

Figure 9 depicts the relationship between area capacitance and frequency. All samples had MnO_2 areal capacitances with CDs, and the doping with Fe and Cu varies slightly between samples, with the MS sample having the highest values. The high areal capacitance at low frequencies is predominantly the response of space charges and drops quickly with increasing frequency.

Conclusion

The synthesis of MnO_2 carbon dots was successfully carried out at low temperatures; no significantly different results are presented by treatment at room temperature and 80 °C. The powder was a poorly crystallized compound resulting from the small grain size. Carbon dots are well adhered to the MnO_2 surface making the core–shell type grains. Mn poses an oxidation state of + 3 and 4 + . The K^+ ionic residue has a large size; it is rather filled between two layers of MnO_6 octahedron chains. The Fe and Cu dopant present in a mixed oxidation state, incorporated in the MnO_2 matrix generating defects Fe'_{Mn}, Cu''_{Mn}, and $V_O^{\cdot\cdot}$. The presence of the oxygen vacancy disrupts the charge mobility resulting in a decrease in the conductivity of doped material.

Supplementary Information The online version contains supplementary material available at https://doi.org/10.1007/s40243-023-00237-4.

Acknowledgements This research is supported by the Indonesian Ministry of Research and Higher Education through the Basic research program managed by DRPM-ITS Contract No. 1376/PKS/ITS/2022.

Data availability Data related to this article is available on demand.

Declarations

Conflict of interest I declare that the work submitted for publication indicated above is original, has not been published before, and is not under consideration for publication anywhere. I declare that there is no conflict of interest concerning this publication. This statement and declaration have been approved by all co-authors.

References

1. Wang, Y., Guo, J., Wang, T., Shao, J., Wang, D., Yang, Y.-W.: Mesoporous transition metal oxides for supercapacitors.

Nanomaterials **5**, 1667–1689 (2015). https://doi.org/10.3390/nano5041667
2. Baral, A., Satish, L., Zhang, G., Ju, S., Ghosh, M.K.: A review of recent progress on nano MnO_2: synthesis, surface modification and applications. J. Inorg. Organomet. Polym. **31**, 899–922 (2021). https://doi.org/10.1007/s10904-020-01823-z
3. Devaraj, S., Munichandraiah, N.: Effect of crystallographic structure of MnO_2 on its electrochemical capacitance properties. J. Phys. Chem. C **112**, 4406–4417 (2008). https://doi.org/10.1021/jp7108785
4. Hatakeyama, T., Okamoto, N.L., Ichitsubo, T.: Thermal stability of MnO_2 polymorphs. J. Solid State Chem. **305**, 122683 (2022). https://doi.org/10.1016/j.jssc.2021.122683
5. Balachandran, D.: First principles study of structure, defects and proton insertion in MnO_2 n.d.:100.
6. Hastuti, E., Subhan, A., Amonpattaratkit, P., Zainuri, M., Suasmoro, S.: The effects of Fe-doping on MnO_2: phase transitions, defect structures and its influence on electrical properties. RSC Adv. **11**, 7808–7823 (2021). https://doi.org/10.1039/D0RA10376D
7. Hastuti, E., Subhan, A., Amonpattaratkit, P., Zainuri, M., Triwikantoro, T., Suasmoro, S.: Oxidation state, local structure distortion, and defect structure analysis of Cu doped α-MnO_2 correlated to conductivity and dielectric properties. Heliyon **8**, e11459 (2022). https://doi.org/10.1016/j.heliyon.2022.e11459
8. Wang, B., Qiu, J., Feng, H., Wang, N., Sakai, E., Komiyama, T.: Preparation of MnO_2/carbon nanowires composites for supercapacitors. Electrochim. Acta **212**, 710–721 (2016). https://doi.org/10.1016/j.electacta.2016.07.066
9. Xia, H., Wang, Y., Lin, J., Lu, L.: Hydrothermal synthesis of MnO_2/CNT nanocomposite with a CNT core/porous MnO_2 sheath hierarchy architecture for supercapacitors. Nanoscale Res. Lett. (2012). https://doi.org/10.1186/1556-276X-7-33
10. Kim, S., Lee, J., Kang, J.S., Jo, K., Kim, S., Sung, Y.-E., et al.: Lithium recovery from brine using a λ-MnO_2/activated carbon hybrid supercapacitor system. Chemosphere **125**, 50–56 (2015). https://doi.org/10.1016/j.chemosphere.2015.01.024
11. Malak-Polaczyk, A., Matei-Ghimbeu, C., Vix-Guterl, C., Frackowiak, E.: Carbon/λ-MnO_2 composites for supercapacitor electrodes. J. Solid State Chem. **183**, 969–974 (2010). https://doi.org/10.1016/j.jssc.2010.02.015
12. Cui, L., Ren, X., Sun, M., Liu, H., Xia, L.: Carbon dots: synthesis, properties and applications. Nanomaterials **11**, 3419 (2021). https://doi.org/10.3390/nano11123419
13. Gao, H., Cao, S., Cao, Y.: Hierarchical core-shell nanosheet arrays with MnO_2 grown on mesoporous $CoFe_2O_4$ support for high-performance asymmetric supercapacitors. Electrochim. Acta **240**, 31–42 (2017). https://doi.org/10.1016/j.electacta.2017.04.062
14. Dixini, P.V.M., Carvalho, B.B., Gonçalves, G.R., Pegoretti, V.C.B., Freitas, M.B.J.G.: Sol–gel synthesis of manganese oxide supercapacitor from manganese recycled from spent Zn–MnO_2 batteries using organic acid as a leaching agent. Ionics **25**, 4381–4392 (2019). https://doi.org/10.1007/s11581-019-02995-6
15. Neelapala, S.D., Shetty, A., Gaggar, G., Mall, R., Dasari, H.: Development of iron doped manganese oxide ($Mn_{2-x}Fe_xO_3$) catalysts for soot oxidation applications. Int. J. Appl. Eng. Res. **13**, 7 (2018)
16. Benedetti, T.M., Gonçales, V.R., Petri, D.F.S., de Torresi, S.I.C., Torresi, R.M.: Macroporous MnO_2 electrodes obtained by template assisted electrodeposition for electrochemical capacitors. J. Braz. Chem. Soc. **21**, 1704–1709 (2010). https://doi.org/10.1590/S0103-50532010000900016
17. Dong, Y., Li, K., Jiang, P., Wang, G., Miao, H., Zhang, J., et al.: Simple hydrothermal preparation of α-, β-, and γ-MnO_2 and phase sensitivity in catalytic ozonation. RSC Adv. **4**, 39167 (2014). https://doi.org/10.1039/C4RA02654C
18. Mondal, J., Srivastava, S.K.: δ-MnO_2 nanoflowers and their reduced graphene oxide nanocomposites for electromagnetic interference shielding. ACS Appl. Nano Mater. **3**, 11048–11059 (2020). https://doi.org/10.1021/acsanm.0c02247
19. Cremonezzi, J.M.O., Tiba, D.Y., Domingues, S.H.: Fast synthesis of δ-MnO_2 for a high-performance supercapacitor electrode. SN Appl. Sci. **2**, 1689 (2020). https://doi.org/10.1007/s42452-020-03488-2
20. Huang, H., Sun, G., Hu, J., Jiao, T.: Low temperature Synthesis of MnO_2/graphene nanocomposites for supercapacitors. J. Chem. **2015**, 1–8 (2015). https://doi.org/10.1155/2015/629362
21. Ji, C., Ren, H., Yang, S.: Control of manganese dioxide crystallographic structure in the redox reaction between graphene and permanganate ions and their electrochemical performance. RSC Adv. **5**, 21978–21987 (2015). https://doi.org/10.1039/C5RA01455G
22. Chen, X., Yan, S., Wang, N., Peng, S., Wang, C., Hong, Q., et al.: Facile synthesis and characterization of ultrathin δ-MnO_2 nanoflakes. RSC Adv. **7**, 55734–55740 (2017). https://doi.org/10.1039/C7RA08962G
23. Zhang, H., Wu, A., Fu, H., Zhang, L., Liu, H., Zheng, S., et al.: Efficient removal of Pb(II) ions using manganese oxides: the role of crystal structure. RSC Adv. **7**, 41228–41240 (2017). https://doi.org/10.1039/C7RA05955H
24. Ilton, E.S., Post, J.E., Heaney, P.J., Ling, F.T., Kerisit, S.N.: XPS determination of Mn oxidation states in Mn (hydr)oxides. Appl. Surf. Sci. **366**, 475–485 (2016). https://doi.org/10.1016/j.apsusc.2015.12.159
25. Beyreuther, E., Grafström, S., Eng, L.M., Thiele, C., Dörr, K.: XPS investigation of Mn valence in lanthanum manganite thin films under variation of oxygen content. Phys. Rev. B (2006). https://doi.org/10.1103/PhysRevB.73.155425
26. Zhan, S., Qiu, M., Yang, S., Zhu, D., Yu, H., Li, Y.: Facile preparation of MnO_2 doped Fe_2O_3 hollow nanofibers for low temperature SCR of NO with NH_3. J. Mater. Chem. A **2**, 20486–20493 (2014). https://doi.org/10.1039/C4TA04807E
27. Araújo, M.P., Nunes, M., Rocha, I.M., Pereira, M.F.R., Freire, C.: Electrocatalytic activity of new Mn_3O_4@oxidized graphene flakes nanocomposites toward oxygen reduction reaction. J. Mater. Sci. **54**, 8919–8940 (2019). https://doi.org/10.1007/s10853-019-03508-6
28. Heath, J.P.: Simulation of impedance spectroscopy in electroceramics using a finite element method n.d.:207